Journal of Materials Chemistry A

ROYAL SOCIETY OF CHEMISTRY

PAPER

View Article Online
View Journal | View Issue

Cite this: J. Mater. Chem. A, 2025, 13, 7515

Ultrafast synthesis of porous Fe_3C/carbon hybrid materials *via* a carbothermal shock reactor for advanced energy storage applications†

Jun Cao,[a] Kai-Yue Ji,[a] Ming-He Du,[a] Chi Zhang,[b] Qi Sun,[c] Ying Yi,[d] Ze-Fan Chai,[a] Chun-Jie Yan[a] and Heng Deng *[ae]

Template-assisted pyrolysis enables the synthesis of Fe-based carbonaceous materials with a defined morphology and structure from iron–carbon precursors. However, conventional tangible templates are costly and have limited applications, and their removal process is time-consuming and environmentally harmful. Here, we employ an ultrafast heating technique (1 second to 1800 °C) using a carbothermal shock reactor to treat iron–carbon precursors. The high-density volatile vapor generated during the rapid pyrolytic carbonization of the precursor acts as a pore-forming agent, resulting in a porous carbon matrix. This high-density vapor also restricts the growth area of iron-based nanoparticles, promoting them to form ultrafine small sizes through confined synthesis. Finally, we successfully prepared the CTS–Fe–C-1800 hybrid material containing a porous carbon matrix and iron carbide nanoparticles and tested its electrochemical performance as a multifunctional electrode. As an electrode, the CTS–Fe–C-1800 supercapacitor (SC) exhibits a high specific capacity of 425.5 F g^{-1} at 0.5 A g^{-1}. Moreover, the CTS–Fe–C-1800 flexible micro-supercapacitor (MSC), prepared using a PVA/KOH gel electrolyte and CTS–Fe–C-1800, demonstrates an impressive energy density of 71.49 W h kg g^{-1} at 0.637 kW kg g^{-1}. Additionally, when employed as an anode electrode in a Li-ion battery (LIB), the CTS–Fe–C LIB maintains a capacity of 801.2 mA h g^{-1} after 1000 cycles at 1 A g^{-1}, surpassing the performance of the majority of reported Fe–C anode electrodes.

Received 3rd August 2024
Accepted 29th January 2025

DOI: 10.1039/d4ta05430j

rsc.li/materials-a

1 Introduction

The rapid development of the global economy, alongside the depletion of fossil fuels and worsening environmental pollution, has sparked considerable interest in sustainable and renewable energy sources.[1,2] Electrochemical energy storage (EES) technology, including supercapacitors (SCs), lithium-ion batteries (LIBs), Zn-ion batteries and potassium-ion batteries, emerges as a promising solution to the power supply challenge due to its notable energy density, power density, and cost-effectiveness.[3,4] Extensive research has been conducted to investigate various energy storage materials, with iron-based materials (such as Fe_3O_4, Fe_2O_3, Fe, and Fe_3C) not only being widely used in the field of catalysis,[5–8] but also attracting significant attention in the field of energy storage materials due to their high theoretical capacity, wide electrochemical window, low cost and abundance.[9,10] However, their practical application is hindered by inadequate electrochemical reactivity and cycling stability. To overcome these challenges, integrating nano-structured iron-based materials into porous carbonaceous materials has demonstrated potential to enhance charge–discharge kinetics and preserve electrode integrity.[11,12] The porous carbon substrate functions as a conductive matrix, preventing nanoparticle aggregation and facilitating ion diffusion and transportation.[13,14] The small and highly dispersed NPs will offer more active sites for the enhanced electrochemical performance. This synergy improves ion-electron transport,[15] enhances electrode/electrolyte contact,[16] and alleviates stress to accommodate volume expansion.[17]

Currently, mainstream methods for preparing iron-based carbonaceous materials typically involve the pyrolysis of iron salt impregnated carbon precursors.[18,19] However, this approach often results in an uncontrolled morphology and structure of the Fe-based nanoparticles (NPs) and porous carbon matrix, leading to inevitable aggregation of iron crystalline nanoparticles and a suboptimal pore structure in the carbon matrix. To overcome this, template-assisted fabrication has been widely adopted to precisely define the morphology and structure of Fe-based NPs

[a]Faculty of Materials Science and Chemistry, China University of Geosciences, Wuhan, 430074, People's Republic of China. E-mail: dengheng@cug.edu.cn
[b]Hangzhou Institute for Advanced Study, University of Chinese Academy of Sciences, Hangzhou 310024, People's Republic of China
[c]College of Materials and Metallurgy, Guizhou University, Guiyang 550025, People's Republic of China
[d]School of Mechanical Engineering and Electronic Information, China University of Geosciences, Wuhan, 430074, People's Republic of China
[e]Shenzhen Research Institute, China University of Geosciences, Shenzhen, 518000, People's Republic of China

† Electronic supplementary information (ESI) available. See DOI: https://doi.org/10.1039/d4ta05430j

and the porous carbon matrix.[20,21] Template-assisted confinement synthesis was adopted to fabricate small-sized and well-defined Fe-based nanoparticles, employing templates to regulate the morphologies and compositions of nanomaterials. For instance, Fe ions can be confined within predefined template structures such as MOFs,[22] carbon nanotubes,[23] or polymer nanofibers.[24] Similarly, templates are employed to synthesize carbon materials with controlled and abundant pores, including hard templates (*e.g.*, SiO_2, Al_2O_3, and MgO)[25] and soft templates[26] (*e.g.*, cellulose, MOFs, and F127), embedded in carbon precursors before carbonization, followed by template removal to yield porous carbon materials. Nonetheless, the utilization of these tangible templates, such as nanoparticles, nanofibers, and polymer networks, poses several challenges. Firstly, these templates can be expensive. Secondly, post-removal of templates to obtain porous carbon materials is time-consuming and often environmentally harmful. Lastly, the distinct templating processes for Fe-based NPs and porous carbon matrices necessitate different types of templates, escalating experimental complexity. Consequently, there is an urgent requirement to develop a simple and highly efficient method for fabricating Fe–C hybrids with defined nanostructures.

Here, we propose utilizing a pore-forming agent-volatile vapor-during pyrolysis to achieve simultaneous pore formation in the carbon matrix and confinement synthesis of Fe-based nanoparticles (NPs). During the pyrolysis of carbon precursors, a significant amount of small molecule vapors are generated, serving both as a pore-forming agent to create porous architectures and as a means to inhibit the fusion of Fe-based NPs, thus constraining their growth. However, traditional pyrolysis processes in tube furnaces often suffer from prolonged heating, leading to pore closure. And the slow heating rate also results in low vapor density, which is insufficient for effective NP confinement. To address these challenges, we employ the ultrafast heating technique of the carbothermal shock reactor, which achieves fast heating to 1800 °C in just 1 second. The rapid carbonization preserves the morphology of porous structures in the carbon matrix, while sharp heating generates high-density vapor steam instantaneously. This dense vapor steam effectively segments the growth domains of Fe-based NPs, confining them and promoting formation into ultrafine and small sizes. By combining these strategies, we aim to achieve precise control over both the porous carbon matrix and the Fe-based NPs, enhancing the performance of iron-based carbon hybrid materials for energy storage applications. Consequently, the CTS–Fe–C-1800 hybrid demonstrates promising electrochemical performances: as electrodes in SCs, it exhibits a good specific capacity of 425.5 F g^{-1} at 0.5 A g^{-1} and an energy density of 148.93 W h kg^{-1} at 1.061 kW kg^{-1}; as an anode in LIBs, it shows the highest capacity of 1485.6 mA h g^{-1} at 0.2 A g^{-1}, with specific capacity retention reaching 100% after 600 cycles.

2 Experimental

2.1 Materials and synthesis

All chemical reagents utilized in this study were procured from commercial suppliers and employed without further purification. The graphite paper was purchased from Senxin Huafeng Co., Ltd. Carbon felt was purchased from Shenzhen Zhongke-Jingyan Technology Co., Ltd. Crocodile clips were purchased from Shenzhen Haoyuan Shengtai Electronics Co., Ltd. Filter paper was purchased from GE Biotechnology (Hangzhou) Co., Ltd. Iron(III) nitrate hydrate ($Fe(NO_3)_3 \cdot 9H_2O$) was purchased from Sinopod Group Chemical Reagent Co., Ltd. 0.3 mm thick nickel foam was purchased from Guangdong Canrd New Energy Technology Co., Ltd. Potassium hydroxide (KOH, AR) was purchased from the Sinopharm group. Silver paint and copper foil tape were purchased from Superior Tape (Hangzhou) Co., Ltd. A polyethylene terephthalate (PET) film was purchased from Ruixin Plastic Industry Co., Ltd. Carbon black and polyvinylidene fluoride (PVDF) were purchased from Hefei Kejing Material Technology Co., Ltd. *N*-Methyl-2-pyrrolidone (NMP), poly(vinyl alcohol) (PVA) (MW = 185 000 g mol L^{-1}, AR), lithium hexafluorophosphate ($LiPF_6$) (97%), ethylene carbonate (EC) (97%), and diethyl carbonate (DEC) (99%) were obtained from Shanghai Aladdin Bio-Chem Technology Co., Ltd.

2.1.1 Preparation of iron-impregnated filter paper (IIFP). Initially, the filter paper was soaked in ethanol and subjected to ultrasonic treatment at 50 Hz for 30 minutes. After washing three times, the treated filter paper was dried in an oven at 60 °C. Next, a solution containing 34.5 g of $Fe(NO_3)_3 \cdot 9H_2O$ dissolved in deionized water was prepared and stirred until the ferric nitrate was completely dissolved, resulting in a 3.5 mol L^{-1} ferric nitrate solution. The dried filter paper was immersed in the ferric nitrate solution at room temperature for 2 hours. Finally, excess iron nitrate solution was removed by placing the filter paper on tissue paper, followed by drying in an oven at 60 °C for 12 hours.

2.1.2 Preparation of CTS–Fe–C samples. The procedure involved cutting the iron-impregnated filter paper (IIFP) into a rectangular film (2 cm × 1 cm) with a geometric area of 2 cm^2. The film was then placed between two layers of carbon paper and heated in the Carbothermal Shock (CTS) reactor at temperatures of 1000 °C, 1400 °C, and 1800 °C, respectively, for approximately 1 second. After CTS processing, the resulting samples were named CTS–Fe–C-1000, CTS–Fe–C-1400, and CTS–Fe–C-1800, respectively.

2.1.3 Preparation of TF–Fe–C samples. The above IIFP rectangular films were placed in a tube furnace (TF), heated to 800 °C at a heating rate of 5 °C min^{-1} under a nitrogen (N_2) atmosphere, and held for 2 hours to obtain the final sample, named TF–Fe–C.

2.1.4 Preparation of SCs and MSCs. The active material, carbon black, and polyvinylidene fluoride (PVDF) were mixed in a mass ratio of 80 : 10 : 10. *N*-Methyl-2-pyrrolidone (NMP) was then added, resulting in a homogeneous slurry after thorough mixing. In this mixture, the as-prepared samples served as the active material, carbon black acted as the conductive agent, PVDF functioned as the binder, and NMP was the solvent. Subsequently, the slurry was applied to nickel foam with a geometric area of 1 cm^2 and dried at 80 °C overnight to evaporate the solvent. Finally, the coated nickel foam was used as the electrodes for the SCs.

In addition, the slurry prepared as described above can also be used as an ink, which was printed onto the surface of a PET film by screen printing as interpolated electrodes for (micro-supercapacitor) MSC assembly, and then dried under vacuum at 60 °C. To facilitate the electrochemical measurement of MSCs, we glued two pieces of copper foil to the end of the interpolated electrodes, coated the connecting part of electrodes and copper foil with silver paint, and then allowed it to dry for 10 minutes. The tape is then placed tightly over the silver paint to avoid direct contact with the electrolyte. The printed electrodes were then coated with a gel-like polymer electrolyte made of 1 mol L^{-1} KOH-PVA. For the preparation of gel electrolytes, we followed the procedure reported in the literature. After drying in the ambient atmosphere, solid coplanar MSCs are formed and stored in a vacuum for further measurement.

2.1.5 Preparation of LIBs. First, the slurry (with the same chemical composition as that used to prepare SC and solid-state MSC electrodes) was coated onto the surface of copper foil. The coated copper foil was then placed in a vacuum drying oven and dried at 70 °C for 12 hours. After drying, the sample was cut into circular sheets with a diameter of 12 mm to serve as the working electrode. In a glove box filled with argon gas (with oxygen and water contents below 0.1 ppm), lithium foil and Crade GF/D were used as the counter electrode and separator, respectively. The working electrode was then assembled into a coin cell (CR2032) with 30 μl of electrolyte (1 M $LiPF_6$ dissolved in a mixture of EC and DEC in a 1 : 1 volume ratio).

2.2 Characterization of microstructures

The phase analysis of the as-prepared samples was performed by X-ray powder diffraction (XRD) using Cu Kα radiation (Bruker AXS, Germany). Microscope images were observed *via* field emission scanning electron microscopy (SEM, HITACHI SU8010, Japan). The SEM system was operated at an accelerating voltage of 20 kV and a working distance ranging from 8 to 15 mm. The size distribution of Fe-based nanoparticles (NPs) was analyzed by selecting 100 randomly selected NPs from the SEM images and processing the data using ImageJ software. For cross-sectional SEM characterization, the samples were cut perpendicular to their plane, with the entire process conducted in liquid nitrogen to achieve a relatively flat cross-section. Elemental composition analysis was conducted using an EDS detector equipped with a HITACHI SU8010 SEM (Japan). A transmission electron microscope (TEM, Tecnai G2 F20, FEI, Netherlands) with an accelerating voltage of 80 kV was used to observe the morphologies of the as-prepared samples. Raman spectroscopy was conducted using a Bruker SENTERRA Raman spectrometer (Germany). The valence states of the elements in the as-prepared materials were analyzed by X-ray photoelectron spectroscopy (XPS) using an ESCALab250 (UK). The Brunauer–Emmett–Teller (BET) method and Barrett–Joyner–Halenda (BJH) method were used to determine the specific surface area and pore size distribution of the as-prepared materials using a BSD-PM2 device (China). Nitrogen adsorption measurements were conducted at 77 K, with all samples degassed for 2 hours at 350 °C prior to the measurements. Thermogravimetric (TG) measurements were conducted using a Netzsch STA2500 apparatus (Germany) with an airflow of 20 mL min^{-1} and a heating rate of 10 °C min^{-1}. A LabRam HR Evolution Raman microscope was used to obtain Raman spectra with a 532 nm excitation laser at a power of 5 mW.

2.3 ReaxFF molecular dynamics (MD) simulation details

First of all, the model was built using the Materials Studio (MS) 2020 software package (BIOVIA, USA). The Forcite Module was used to optimize the molecular structure with COMPASSII as the force field. During the geometric optimization process, the convergence thresholds for maximum energy change, maximum force convergence threshold, and maximum displacement convergence threshold are 0.001 kcal mol^{-1}, 0.5 kcal mol^{-1} $Å^{-1}$, and 0.015 Å, respectively, to release internal stress in the system. In order to obtain a more optimized structure, a 500 ps dynamic simulation was conducted under the NVT ensemble with a step size of 1 fs at 298.15 K. During MD simulations, electrostatic interactions are calculated using Ewald, while van der Waals forces are calculated using atom base. The precise Nose–Hoover temperature control mode and Berendsen pressure control mode are used in the dynamic process.

The procedure used for simulation of the polymer involved minimization of each structure using low-temperature MD. Next, all structures were equilibrated at different temperatures (1000 °C, 1400 °C, and 1800 °C) using NVT-MD simulation (using a Berendsen thermostat) and a time step of 0.05 fs with the following exceptions: in ReaxFF simulation, the temperature of the model was increased from room temperature to 1000 °C in a time of 500 ps and maintained at 1000 °C in a time of 500 ps, and then maintained at 1000 K for 50 ps. After the simulation is completed, the amount of CO_2 generated is counted as a function of temperature. The bond order cutoff for molecule recognition used in the analysis of all systems was 0.3 Å.

3 Results and discussion

3.1 Preparation and characterization

Ultrafast pyrolysis is achieved using the CTS reactor, constructed by tightly packing two joule-heating carbon papers together, as illustrated in Fig. 1. The reactant is sandwiched between the two carbon papers (Fig. S1†). By applying a high density of current passing through the carbon papers, ultrafast radiation heating is achieved between them, resulting in rapid pyrolysis. As shown in Fig. 1, the CTS reactor reaches temperatures of approximately 1800 °C within 1 second (with an initial input of approximately 410 mg, the yield obtained per experiment was about 80 mg), accompanied by a noticeable and intense flash of light (Movie S1†). To conceptually validate this approach, we utilize a well-established example of pyrolyzing iron-impregnated filter paper in our CTS reactor. Previous literature studies indicate that iron-impregnated filter paper can be pyrolyzed into iron–carbon hybrids in tube furnaces or muffle furnaces,[27] with potential applications in SCs and LIBs.[28,29] However, low Fe ion loading reduces the content of

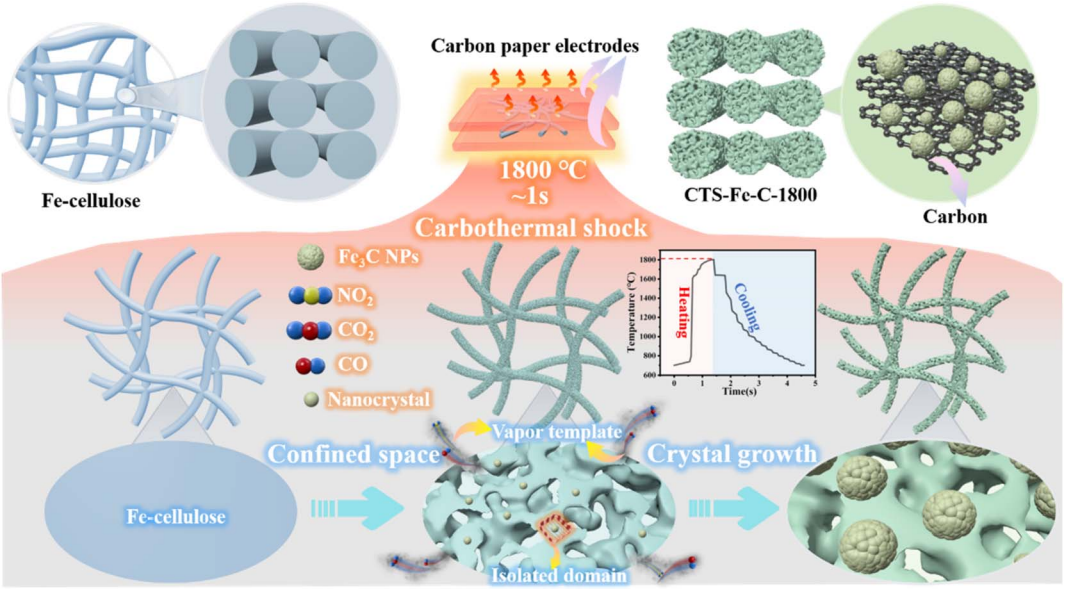

Fig. 1 Schematic illustration of the CTS–Fe–C-1800 sample on the CTS reactor.

electrochemically active Fe species, compromising performance, while high Fe ion loading can lead to the aggregation of iron-based nanoparticles, negatively affecting material properties. To address this, our work builds upon prior research by adopting an optimal iron ion loading for the experiment.[27] To do this, commercial laboratory filter paper is soaked in an iron nitrate solution for 4 hours to ensure absorption of iron ions. After drying, the iron-impregnated filter paper is placed between the two joule-heating carbon electrodes for subsequent CTS pyrolysis.

Following pyrolysis in the CTS reactor at 1800 °C, the original deep yellow iron-impregnated filter paper (IIFP) turns black (Fig. S2†), indicating the carbonization of the filter paper, referred to as CTS–Fe–C-1800. As depicted in Fig. 2a, CTS–Fe–C-1800 maintains the original interconnected fiber structures of the filter paper (Fig. S3†), with the formation of numerous pore (micropores and small mesopores) structures within the fibers (Fig. 2a–c). This is attributed to the predominant cellulose composition of the filter paper. During cellulose pyrolysis, volatile gases, including CO_2 and CO are released.[30] Furthermore, Fe $(NO)_3$ decomposes to release NO_2 and H_2O gases.[31,32] These volatile gases act as a pore-forming agent, creating voids within the resulting carbon structure and thereby forming pore structures in the carbon matrix. To emphasize the distinctive features of ultrafast pyrolysis facilitated by the CTS reactor, we conducted traditional slow pyrolysis of the same iron-impregnated filter paper in a tube furnace (TF) under a N_2 atmosphere for comparison. The obtained TF heating process were obtained from previous literature studies,[27] and the resulting products were labeled as TF–Fe–C. While TF–Fe–C also displays a porous fibrous structure (Fig. 2d), noticeable differences in morphology between TF–Fe–C and CTS–Fe–C-1800 are evident. Firstly, CTS–Fe–C-1800 exhibits a more dispersed fiber structure, contrasting sharply with the fused fiber structure observed in TF–Fe–C. This variation arises from the distinct heating profiles of the respective reactors. In the tube furnace, characterized by a slow heating rate, cellulose fibers within the filter paper gradually melt and fuse at low temperatures, followed by carbonization at elevated temperatures.[33] In contrast, the ultrafast heating rate of the CTS reactor bypasses the low-temperature heating phase, facilitating direct carbonization of the cellulose fibers while maintaining the original dispersed fiber structure, as evidenced by SEM images of the raw filter paper (Fig. S3†). Secondly, the surface morphology of CTS–Fe–C-1800 fibers displays pronounced porosity, whereas TF–Fe–C surfaces appear dense and smooth (Fig. 2e and f). This difference in surface characteristics can be also attributed to the distinct heating rates employed in the two methods. During cellulose pyrolysis, volatile compounds undergo vaporization, resulting in pore formation within the final carbon products. However, in the tube furnace, the slow heating rate promotes material fusion, leading to pore closure before carbonization occurs. Conversely, the rapid heating process in the CTS reactor preserves the porous structure, thereby maximizing pore retention in the carbon products (Fig. 2g).

Additionally, a notable distinction lies in the Fe-based nanoparticles (NPs) embedded within the carbon matrix. In the TF–Fe–C hybrid, NPs measuring approximately 180 nm (calculation from Fig. 2e) in size were formed within the carbon fibers (Fig. 2h), whereas in the CTS–Fe–C hybrid, the resulting NPs were much smaller (Fig. 2i), averaging around 15 nm (calculation from Fig. 2b). The generation of small NPs can be ascribed to the ultrafast pyrolysis process characterized by rapid heating and cooling rates. Analogous to other non-equilibrium fabrication methods like laser fabrication,[34,35] microwave fabrication,[36] or flash joule heating,[37] where reactions occur within a very short timeframe, NP growth is effectively

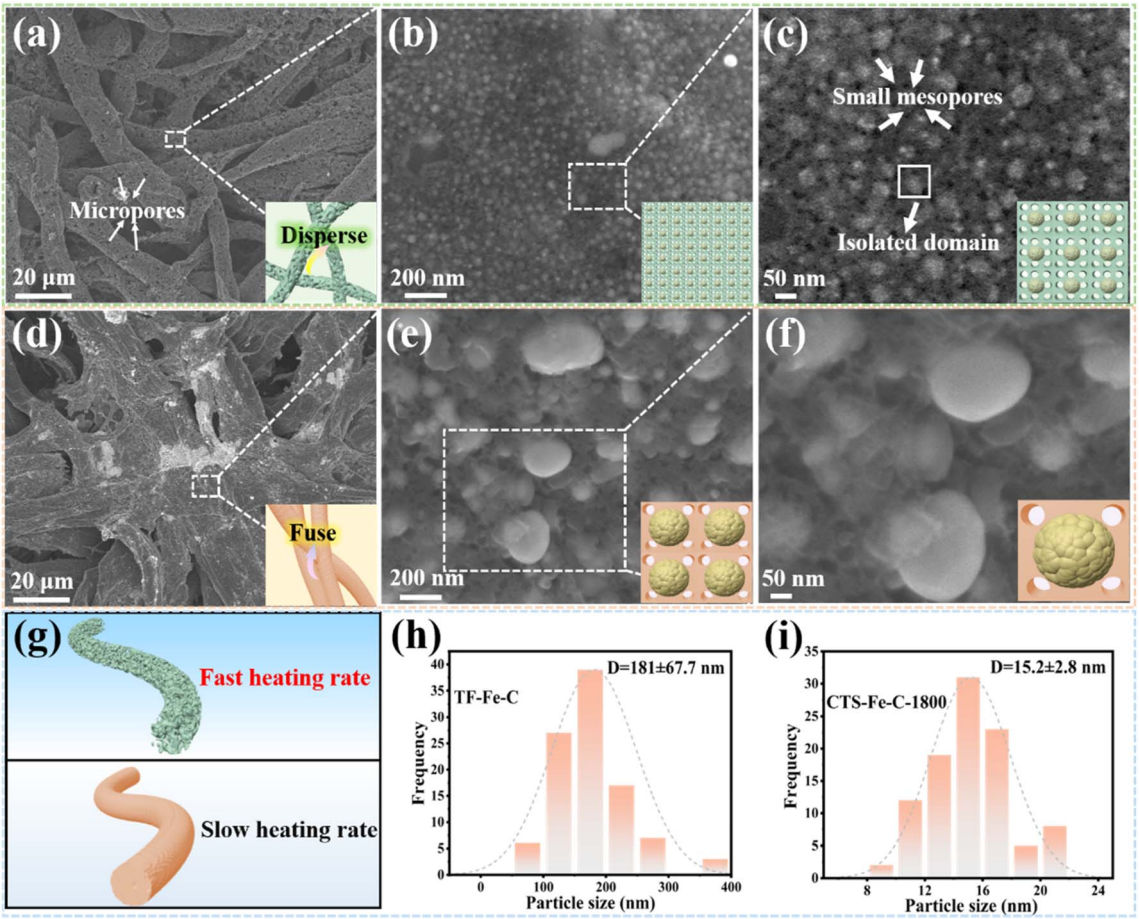

Fig. 2 (a–c) Low and high magnified SEM images of CTS–Fe–C-1800. (d–f) Low and high magnified SEM images of TF–Fe–C. (g) Morphological difference between CTS–Fe–C-1800 and TF–Fe–C. (h) NP size distribution diagram of TF–Fe–C. (i) NP size distribution diagram of CTS–Fe–C-1800.

constrained, leading to the formation of small and uniform NPs. However, in our investigation, the formation of small NPs was not solely attributed to the short reaction duration but also involved the templating effect of volatile vapor during pyrolysis. We observed that reducing the maximum temperature of the CTS reactor to 1400 °C and 1000 °C resulted in the production of CTS–Fe–C-1400 (Fig. 3a–c) and CTS–Fe–C-1000 (Fig. 3d–f) products, respectively, featuring considerably larger NPs, approximately 260 nm (calculation from Fig. 3a) and 490 nm (calculation from Fig. 3d) in size. It is noteworthy that the reaction still occurred within the short duration of 1 second (Fig. S4†). In principle, when the reaction occurs rapidly, NP growth is expected to be constrained, leading to the formation of small and uniform NPs. However, the size of NPs in CTS–Fe–C-1400 and CTS-Fe-1000 exceeded that of TF–Fe–C, fabricated using the TF reactor.

This unusual experimental observation can be attributed to the following reasons: in the traditional gradual pyrolysis process in the TF, $Fe(NO)_3$ begins to decompose into NO_2 and H_2O at low temperatures,[38] initiating the formation of Fe-based nanocrystals, while cellulose remains uncarbonized. These nanocrystals were adhered to the cellulose matrix, being stabilized and dispersed by it. As the temperature gradually increases, the nanocrystals undergo Ostwald ripening, leading to an increase in size and eventually forming large nanoparticles (NPs). In contrast, during the CTS pyrolysis process, the temperature rapidly exceeds 1000 °C. At this high temperature, the decomposition of $Fe(NO)_3$ and the carbonization of cellulose occur simultaneously, resulting in the immediate generation of a significant amount of volatile vapor. On the one hand, the instant mass of volatile vapor creates a non-equilibrium and chaotic reaction environment, potentially facilitating the mixing and fusion of the Fe-based nanocrystals, leading to the formation of larger NPs. On the other hand, the volatile vapor acts as a pore-forming agent for creating voids within the formed carbon matrix. These voids partition the carbon matrix into separate domains, providing sites for NP anchoring. The size of the NPs is constrained by the dimensions of these isolated domains. Consequently, as more volatile vapor is generated and more porous structures are formed, NPs are confined to smaller sizes.

By increasing the reaction temperature in the CTS pyrolysis process, a greater amount of volatile vapor is generated, as evidenced by the observed mass loss during pyrolysis.

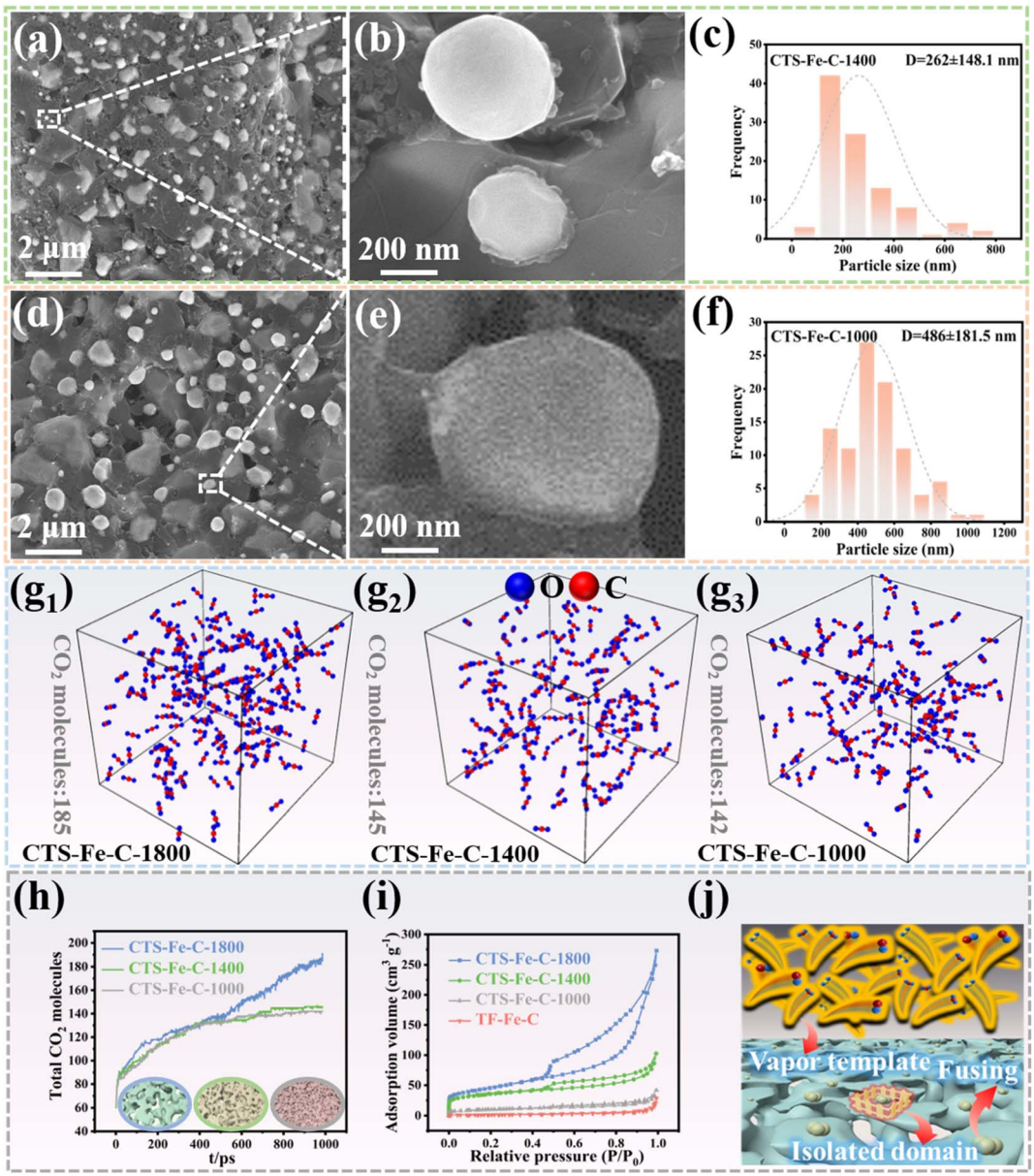

Fig. 3 (a and b) Low and high magnified SEM images of CTS–Fe–C-1400. (c) NP size distribution diagram of CTS–Fe–C-1400. (d and e) Low and high magnified SEM images of CTS–Fe–C-1000. (f) NP size distribution diagram of CTS–Fe–C-1000. (g and h) ReaxFF MD simulates the generation of CO_2 molecules during the formation of CTS–Fe–C-1800, CTS–Fe–C-1400 and CTS–Fe–C-1000. (i) N_2 adsorption–desorption isotherms of Fe–C samples. (j) Formation mechanism of CTS–Fe–C-1800.

Specifically, CTS–Fe–C-1800 exhibits the highest pyrolysis mass loss (Fig. S5†), indicating the most significant vapor generation. Although direct observation of small molecule vapor generation *in situ* is challenging, we conducted molecular dynamics (MD) simulations to simulate the pyrolysis process within the CTS reactor (Fig. 3g and h). To simplify the simulation process, we incorporated only 10 cellulose molecules into the system and examined the generation of total pyrolysis products generated at different temperatures (1000 °C, 1400 °C, and 1800 °C) (Fig. S6†). During the pyrolysis process, small molecule vapors are produced. To simplify the analysis, CO_2 was selected as a representative molecule for the total small molecule vapor. The amount of CO_2 generated at different CTS pyrolysis temperatures was quantified (Fig. 3h). The simulation results show that the number of CO_2 molecules increases with increasing temperature, with a significantly higher production of CO_2 at 1800 °C compared to 1000 °C and 1400 °C. This suggests that more volatile vapors are generated with higher temperature treatments, which aligns with our experimental findings. As a result of increased volatile vapor generation, the porosity of the products increases, resulting in an increase in their specific surface areas (Fig. 3i, j and Table S1†). BET analysis reveals that CTS–Fe–C-1800 exhibits the highest specific surface area of 161.3 $m^2 g^{-1}$, whereas CTS–Fe–C-1400, CTS–Fe–

C-1000 and TF–Fe–C exhibit specific surface areas of 118.1 m^2 g^{-1}, 35 m^2 g^{-1} and 5.8 m^2 g^{-1}, respectively. Moreover, SEM images exhibit a significantly more porous morphology in CTS–Fe–C-1800 (Fig. 2c) compared to CTS–Fe–C-1400 and CTS–Fe–C-1000. The pore structures in CTS–Fe–C-1800 are notably denser and divide the carbon matrix into smaller domains. Within each domain, small NPs are anchored, surrounded by a network of pores within the carbon matrix, indicating that the size of NPs is constrained by the surrounding pore structures (Fig. 2c). These findings collectively suggest that the ultrafast and high-temperature heating of the CTS reactor enables volatile vapor to act as a pore-forming agent, facilitating simultaneous pore formation in the carbon matrix and confinement synthesis of Fe-based NPs. TEM images also showed significantly smaller Fe-based NPs in CTS–Fe–C-1800 (Fig. S7a†) compared to CTS–Fe–C-1400 (Fig. S8a†) and CTS–Fe–C-1000 (Fig. S9a†).

To analyze the structures and compositions of the obtained Fe–C hybrids, we employed X-ray diffraction (XRD). As shown in Fig. 4a–c, the TF hybrids exhibit prominent XRD peaks at 2θ = 26.8° and 42.2°, corresponding to the (002) and (400) planes of graphite and Fe_3O_4,[39] respectively. For the CTS–Fe–C hybrids, new XRD peaks at 2θ = 38.0°, 43.8°, and 64.8° appeared, attributed to the (210), (102), and (321) planes of Fe_3C[40] This may result from the more severe reaction conditions in the CTS reactor, where iron ions could directly react with the carbon precursor to generate carbide.[41,42] In CTS–Fe–C-1800, due to the high temperature, almost all iron ions are transformed into Fe_3C. It should be noted here thar the 2θ = 64.8° peak could refer to the (321) plane of Fe_3C or the (200) plane of metallic Fe. To clarify the attribution of this XRD peak, we conducted thermogravimetric (TG) analysis of these samples (Fig. 4d). If Fe exists in these hybrids, there should be a slight weight increase from 190 °C to 410 °C due to the oxidation reaction of metallic Fe to Fe_2O_3.[43] However, in the TG curves of these CTS–Fe–C hybrids, no such weight increase is observable, indicating that these peaks undoubtedly belong to Fe_3C. The proportional composition of different iron phases in the Fe–C composites was ascertained through Rietveld refinement of the XRD data using Jade software. Combined with the TG results, the proportional composition of carbon, Fe_3O_4, and Fe_3C in these

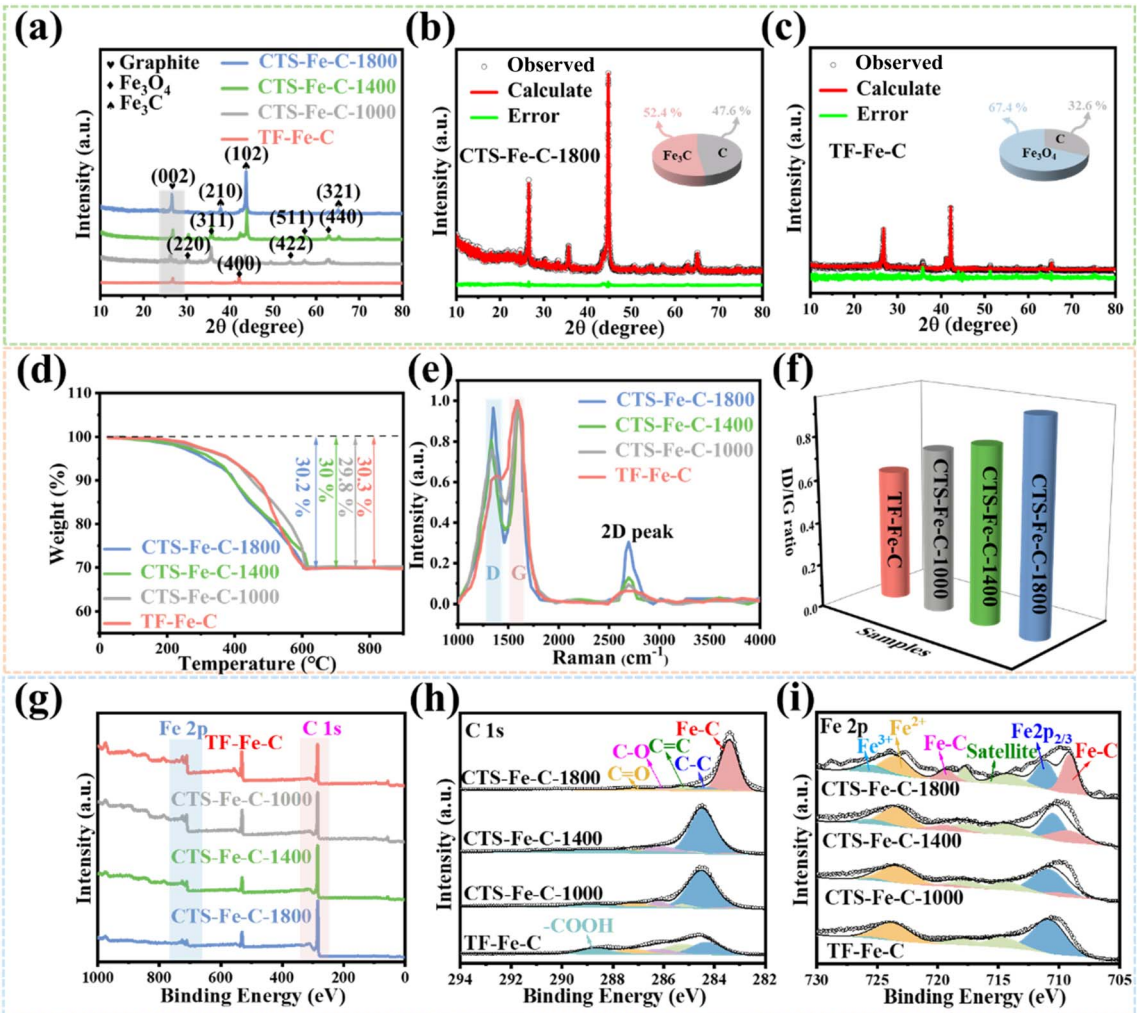

Fig. 4 (a) XRD patterns of Fe–C samples. (b) XRD patterns and Rietveld refinement of CTS–Fe–C-1800. (c) XRD patterns and Rietveld refinement of TF–Fe–C. (d) TG curves of Fe–C samples. (e and f) Raman spectra and I_D/I_G values of Fe–C samples. (g) XPS survey of Fe–C samples. (h and i) High-resolution XPS surveys of C 1s and Fe 2p, respectively.

Fe–C hybrids could be calculated, as shown in Fig. 4b, c and S10, S11.† Details of the calculation can be found in the ESI.† Moreover, there are other noticeable differences in these XRD spectra. CTS–Fe–C hybrids exhibit an obvious graphitic peak at $2\theta = 26.8°$, while TF–Fe–C did not show such a peak. This suggests that the carbon composition in TF–Fe–C is amorphous. In CTS–Fe–C hybrids, due to non-equilibrium and extreme reaction conditions, graphitization of the carbon precursor is more likely to occur.

To further analyze the carbon materials, Raman spectroscopy is a powerful tool. Raman spectroscopy analysis demonstrates the consistent presence of the D band at 1351 cm^{-1} indicative of defective graphitic carbon and the G band at 1590 cm^{-1} representing sp^2-hybridized carbon across all samples (Fig. 4e).[44] However, the TF–Fe–C sample exhibits broader D and G peaks, suggesting a more amorphous carbon structure.[45,46] Additionally, a broad peak ranging from 2500 to 3000 cm^{-1}, corresponding to the combination mode of D + D′,[45] further supports the amorphous nature of carbon in TF–Fe–C. In contrast, CTS–Fe–C hybrids display sharper D and G peaks, indicating enhanced graphitization, consistent with XRD results. Furthermore, the appearance of a small 2D band at 2695 cm^{-1} suggests the presence of few-layer graphene in these samples. These findings indicate the role of the CTS reactor in providing intense and non-equilibrium reaction conditions, which is conducive to improved graphitization. Moreover, the higher temperatures in the CTS reactor led to an increased I_D/I_G ratio (Fig. 4f), signifying higher defect generation due to the increasing volatile vapor production during pyrolysis. These defects may facilitate mass and ion transportation efficacy when these materials are utilized as electrode materials.[47]

The bonding characteristics and elemental composition of Fe–C hybrids are confirmed with X-ray photoelectron spectroscopy (XPS) (Fig. 4g). The XPS spectra of C 1s revealed distinct peaks at 284.4 eV, 285.2 eV, and 286.2 eV in the C 1s region, corresponding to C–C, C=C, and C–O bonds, respectively (Fig. 4h). Additionally, in the CTS–Fe–C hybrid, a discernible Fe–C peak at 283.4 eV was observed, indicative of Fe_3C formation. Notably, in the CTS–Fe–C-1800 sample, where the majority of Fe ions existed in the Fe_3C state, the Fe–C peak predominated. This observation was further corroborated by the Fe 2p XPS spectra (Fig. 4i), where only the CTS–Fe–C-1800 sample exhibited a significantly dominant Fe–C peak at 708.9 eV and 719.1 eV. These findings align closely with XRD results, which confirmed the presence of Fe-based NPs in the Fe_3C phase within the CTS–Fe–C-1800 sample. Moreover, the composite structure of the Fe–C hybrid materials was further investigated using transmission electron microscopy (TEM). TEM imaging of the CTS–Fe–C-1800 sample corroborated the uniform distribution of nanoparticles encapsulated within the carbon layer, consistent with observations from SEM analysis (Fig. S7a†). High-resolution TEM (HRTEM) analysis revealed lattice fringes in the samples. Specifically, in CTS–Fe–C-1800 (Fig. S7b and c†), the carbon layer exhibited high crystallinity, displaying a lattice spacing of 0.34 nm, corresponding to the (002) crystal face of graphitic carbon (JCPDS #41-1487), while the lattice spacing of 0.24 nm and 0.21 nm in the nanoparticles corresponded to the (210) and (102) crystal planes of Fe_3C (JCPDS #35-0772), respectively, confirming the presence of Fe_3C nanoparticles. Furthermore, TEM analysis of CTS–Fe–C-1400 (Fig. S8b and c†) and CTS–Fe–C-1000 (Fig. S9b and c†) revealed lattice fringes corresponding to graphitic carbon, Fe_3C crystal faces, as well as Fe_3O_4 (220) crystal faces (JCPDS #76-1849). Energy dispersive X-ray spectroscopy (EDS) elemental maps obtained in STEM mode illustrated the uniform distribution of Fe_3C nanoparticles within the carbon matrix (Fig. S12†).

3.2 Electrochemical properties

The characterization and analysis above indicate that the CTS–Fe–C-1800 hybrid exhibits a large specific surface area, characterized by abundant pore structures and small-sized NPs. This morphology is advantageous for facilitating mass or ion transportation when it was utilized as an electrode material.[48] Moreover, the formation of Fe_3C NPs enhances the electrochemical performance, making them suitable for applications in SCs and LIB electrodes.[40] Therefore, the potential of CTS–Fe–C-1800 as an electrode material for SCs and LIBs was assessed, along with other Fe–C hybrids for comparison. The electrochemical performance of sample-based SCs (Fig. 5a) was compared using CV (Fig. 5b and S13†) curves and GCD (Fig. 5c and S14†) curves ranging from −1.0 to 0 V in a three-electrode structure with a 1 M KOH aqueous electrolyte. The CV areas of the CTS–Fe–C-1800 SC are larger than those of CTS–Fe–C-1400, CTS–Fe–C-1000 and TF–Fe–C SCs at a scan rate of 1–20 mV s^{-1}. Generally, the area of the CV curve is proportional to the specific capacitance. Therefore, the CTS–Fe–C-1800 SC has the largest capacitance compared to other samples. Then, the discharge times of CTS–Fe–C-1800 SC are significantly longer than those of the other three samples at various current densities. Undoubtedly, CTS–Fe–C-1800 SC (323.3 F g^{-1} or 6.5 mF at 1 A g^{-1}, 148.9 W h kg^{-1} at 1.061 kW kg^{-1} or 0.046 mW h cm^{-2} at 0.255 mW cm^{-2} *via* eqn (S1)–(S6)†) also exhibited the highest specific capacity (Fig. 5d and S15†) and energy density (Fig. S16†) compared to CTS–Fe–C-1400, CTS–Fe–C-1000 and TF–Fe–C SCs. This performance is also comparable to that of most reported Fe_3C-based SCs (Table S2†). The better specific capacitance and energy density of the CTS–Fe–C-1800 SC, compared to CTS–Fe–C-1400, CTS–Fe–C-1000, and TF–Fe–C SCs, can be attributed to the following factors. First, CTS–Fe–C-1800 SC possesses a higher specific surface area compared to CTS–Fe–C-1400, CTS–Fe–C-1000 and TF–Fe–C SCs, which provides an increased number of active sites for charge storage.[48] Additionally, the CTS–Fe–C-1800 SC showed a higher degree of graphitized carbon (Fig. 4f) than CTS–Fe–C-1400, CTS–Fe–C-1000 and TF–Fe–C, therefore offering a more conductive carbon matrix,[40] which can be seen from the electrochemical impedance spectroscopy (EIS) data. As shown in Fig. 5e, the CTS–Fe–C-1800 SC shows the lowest series resistance (R_s) value of 1.48 Ω, which facilitates more efficient charge transfer.[49]

We further examined the charge storage mechanism of SCs through CV curves. All SCs were fitted based on the peak oxidation currents at different scanning rates (Fig. S13†), and

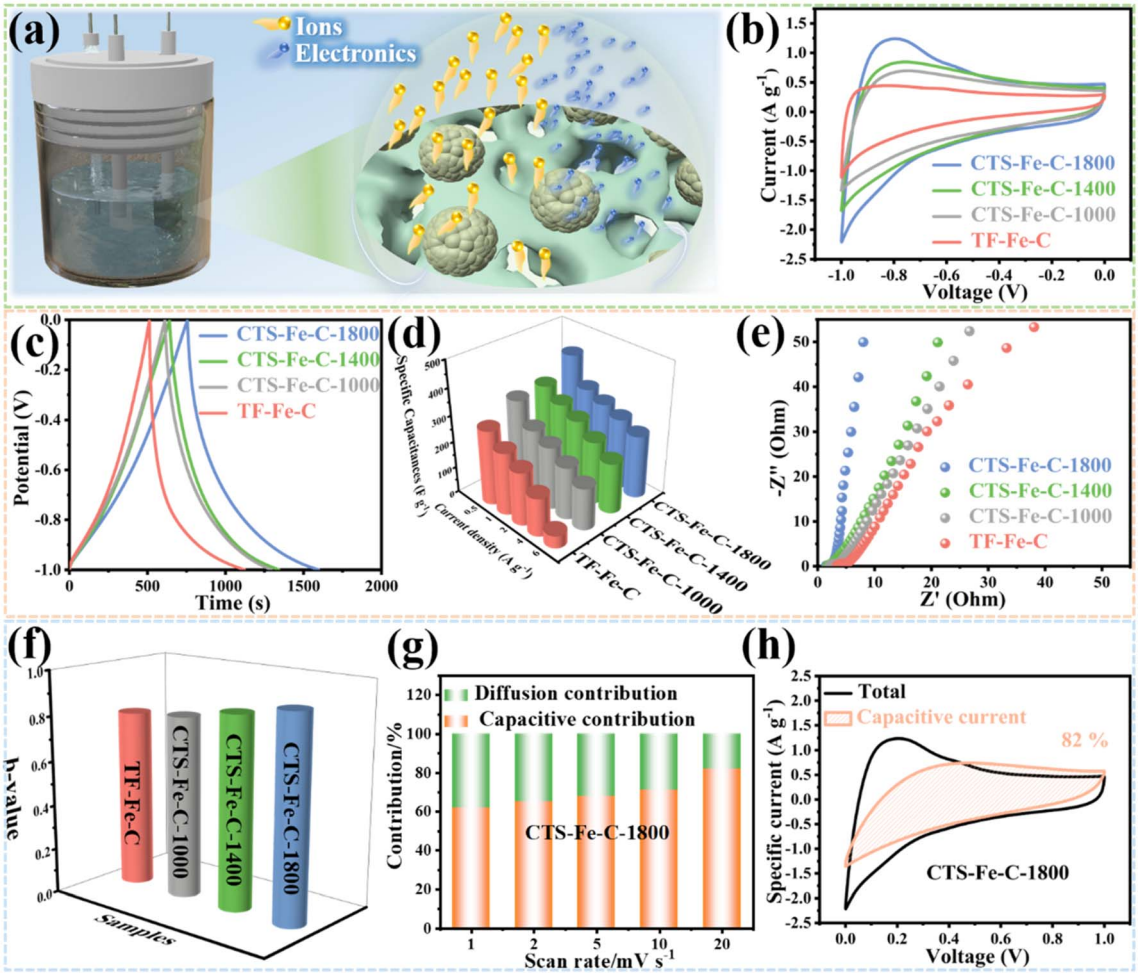

Fig. 5 Electrochemical performance of supercapacitors (SCs). (a) Schematic illustration of the three-electrode structure SC. (b) CV curves of Fe–C SCs at a scan rate of 20 mV s^{-1}. (c) GCD curves of Fe–C SCs at a current density of 0.5 A g^{-1}. (d) Specific capacitance of Fe–C SCs at different current densities. (e) Nyquist plots of Fe–C SCs. (f) The *b* values of Fe–C SCs. (g and h) Contribution percentages of the capacitive and diffusion-controlled process at different scan rates of the CTS–Fe–C-1800 SC.

the *b* values were determined to be 0.79 (TF–Fe–C SC), 0.81 (CTS–Fe–C-1000 SC), 0.86 (CTS–Fe–C-1400 SC), and 0.91 (CTS–Fe–C-1800 SC) *via* eqn (S7) (Fig. 5f and S17†). These *b* values, ranging between 0.5 and 1, indicate that all SCs exhibit both diffusion and capacitance control during the electrochemical process. Specifically, the *b* value of the CTS–Fe–C-1800 SC is closest to 1, suggesting that it predominantly exhibits pseudocapacitive behavior, with its electrochemical processes primarily governed by capacitive control.[50] We further quantified the capacitance contribution for all SCs using eqn (S8)† as shown in Fig. 5g, h and S18.† In particular, the capacitance control of CTS–Fe–C-1800 SC increases from 62% to 82% as the scan rate increases from 1 mV s^{-1} to 20 mV s^{-1}. Moreover, the CTS–Fe–C-1800 SC consistently demonstrated a higher capacitance control than the other samples across all scan rates, aligning well with the *b*-value analysis. The high capacitance control ratio of the CTS–Fe–C-1800 SC can be attributed to its small and uniformly distributed Fe_3C NPs.[51]

The feasibility of fabricating flexible MSCs using CTS–Fe–C-1800 through screen printing was investigated. As shown in Fig. 6a, the CTS–Fe–C-1800 ink was deposited onto a PET film in an interdigitated pattern, followed by the application of a PVA/KOH gel electrolyte to create the MSC. The electrochemical performance of the assembled CTS–Fe–C-1800 MSC was investigated by recording their CV and GCD curves. Notably, the peak positions shifted only slightly when the scan rate increased from 1 to 20 mV s^{-1} (Fig. 6b), indicating the good reversibility of the devices. The GCD curve and specific capacity of the MSC are shown in Fig. 6c, d and S19,† which exhibits the highest specific capacity of 204.2 F g^{-1} (3.8 mF cm^{-2}) at a current density of 0.5 A g^{-1}, and even at a current density of 6 A g^{-1}, the MSC still maintains a specific capacity of 115.2 A g^{-1} (2.1 mF cm^{-2}). The CV curves under various bending conditions (Fig. 6e and f) demonstrated no significant changes, confirming the device's mechanical flexibility and suitability for practical applications. The Ragone plot in Fig. S20† illustrates the energy density and power density of the MSC. The device exhibited an energy

density of 71.49 W h kg^{-1} at 0.637 kW kg^{-1} (0.02 mW cm^{-2} at 0.08 mW h cm^{-2}). As depicted in Fig. S20a,† the energy density of the device surpasses that of most reported Fe_3C-based MSCs (Table S3†). Furthermore, the long-term cycle stability of the device was evaluated. As depicted in Fig. 6g, after 180 h operation in floating mode, the capacity of the MSC remains at 187.3 F g^{-1}, demonstrating its long-term cycle stability. Moreover, the cycled CTS–Fe–C-1800 electrode was also analyzed using FESEM (Fig. S21a and b†), HRTEM (Fig. S21c†), XRD (Fig. S22a†), and XPS (Fig. S22b–d†). The results show that the structure of the electrode remains stable, with no significant changes in its chemical composition or morphology. Additionally, three CTS–Fe–C-1800 MSCs were connected in series, and the CV and GCD curves of a single device and three devices connected in series were obtained at the same current density, as depicted in Fig. 6h and i. The capacitance of the series-connected devices

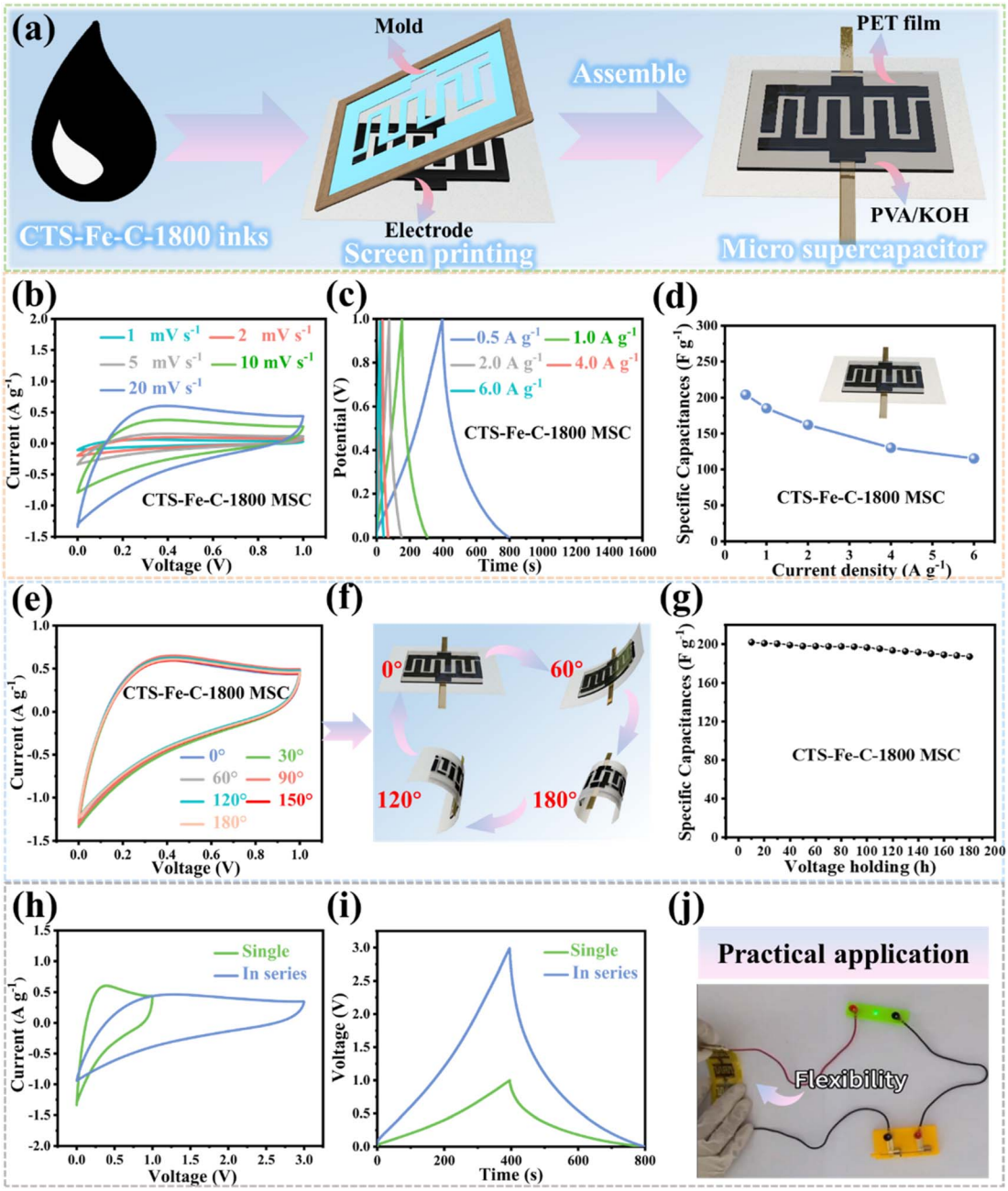

Fig. 6 Electrochemical performance of micro-supercapacitors (MSCs). (a) Schematic illustration of CTS–Fe–C-1800 MSC preparation. (b) CV curves of the CTS–Fe–C-1800 MSC at different scan rates. (c) GCD curves of the CTS–Fe–C-1800 MSC at different current densities. (d) Specific capacitance of the CTS–Fe–C-1800 MSC at different current densities. (e and f) CV curves and capacitance retention of the CTS–Fe–C-1800 MSC under bending angles from 0° to 180° at 20 mV s^{-1}. (g) The specific capacitance as a function of the floating time. (h) CV curves at a scan rate of 20 mV s^{-1} for a single CTS–Fe–C-1800 MSC and multiple CTS–Fe–C-1800 MSCs connected in series. (i) GCD curves at a current density of 0.5 A g^{-1} for a single CTS–Fe–C-1800 MSC and multiple CTS–Fe–C-1800 MSCs connected in series. (j) Optical image of a green LED bulb powered by three serially connected CTS–Fe–C-1800 MSCs.

significantly increases compared to the single device, and the output voltage range expands from 0–1 V to 0–3 V. In the bending state, the series-connected device can illuminate a green LED (3.0 V) (Fig. 6j and Movie S2†). Therefore, the above results indicate that the CTS–Fe–C-1800 MSC shows promise as a component for flexible power supplies for wearable and portable devices.

The electrochemical performance of Fe–C hybrids as LIB anode electrode materials was examined, as depicted in Fig. 7a. The CV curves for the initial three cycles of the CTS–Fe–C-1800 LIB are shown in Fig. 7b. In the first cycle, a sharp reduction peak below 0.1 V is observed in the initial cathodic process, attributed to the formation of a solid electrolyte interface (SEI) layer. In the subsequent charge process, a broad peak at about 1.75 V appears in the first anodic curve, representing the reversible oxidation reactions of the partial SEI catalyzed by Fe_3C (Fig. S23†).[52] From the second cycle, the cathodic peak at 0.5 V shifts to approximately 0.7 V, and the anodic peak moves slightly to a higher potential (approximately 1.9 V) as well. Meanwhile, an apparent decrease in cathodic current is

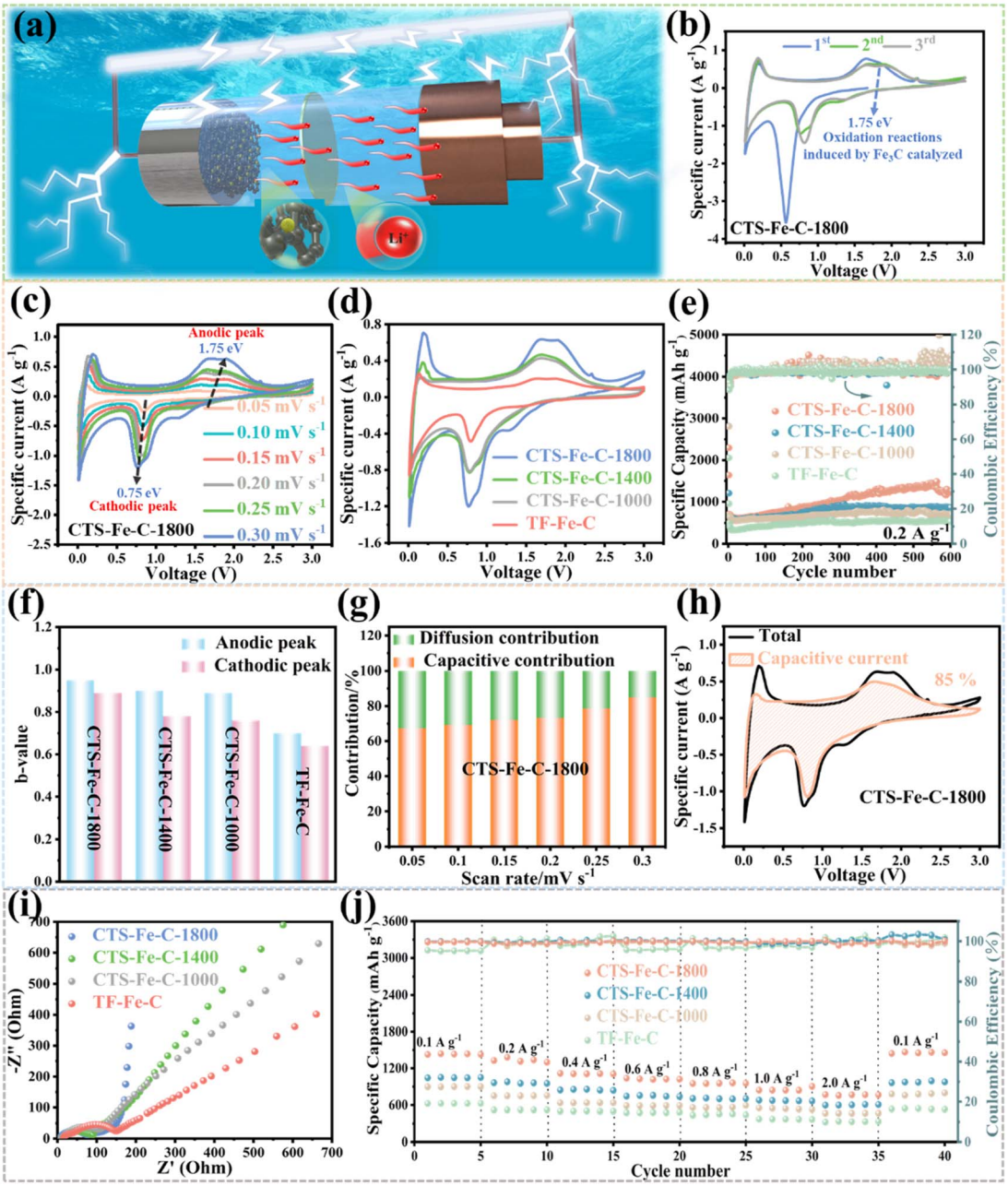

Fig. 7 Lithium-ion storage performance. (a) Schematic illustration of the CTS–Fe–C-1800 LIB. (b) CV curves of the CTS–Fe–C-1800 LIB, recorded at 0.30 mV s^{-1}. (c) CV curves of the CTS–Fe–C-1800 LIB at different scan rates. (d) CV curves of Fe–C LIBs at 0.30 mV s^{-1}. (e) Cycling performance of Fe–C LIBs at 0.2 A g^{-1}. (f) The *b* values of Fe–C LIBs. (g and h) Contribution percentages of the capacitive and diffusion-controlled process at different scan rates of the CTS–Fe–C-1800 LIB. (i) Nyquist plots of Fe–C LIBs. (j) Rate performance of Fe–C LIBs.

observed in the second CV curve compared with the first one, indicating specific capacity loss after the first discharge/charge process due to SEI film formation and an irreversible lithium insertion reaction. From the second and third cycle, the CV curves nearly overlap, indicating the reversibility and electrochemical stability of the anode made from CTS–Fe–C-1800. As depicted in Fig. 7c, the peaks retain well-defined configurations even with an increase in the scan rate from 0.05 mV^{-1} to 0.30 mV^{-1}, demonstrating the good reversibility of the SEI. Similar to the above results of the supercapacitor application, the CTS–Fe–C-1800 LIB also exhibits a better performance than CTS–Fe–C-1400, CTS–Fe–C-1000, and TF–Fe–C LIBs, due to the smaller and more uniformly distributed Fe_3C NPs and a more porous carbon matrix. As shown in Fig. 7d and S24,† the CV geometric area of the CTS–Fe–C-1800 LIB is significantly higher than that of CTS–Fe–C-1400, CTS–Fe–C-1000, and TF–Fe–C LIBs.

The cycling performance of these LIBs at 0.2 A g^{-1} is tested and shown in Fig. 7e. The CTS–Fe–C-1800 LIB demonstrates the highest initial discharge specific capacity of 1639.2 mA h g^{-1}. Subsequently, the discharge specific capacity of all LIBs decays faster initially and then increases slowly. This phenomenon is attributed to the gradual release of additional Li ions stored in the SEI layer during prolonged cycling, providing additional specific capacity. During the cycling process, the CTS–Fe–C-1800 LIB consistently exhibits the highest discharge specific capacity, reaching a peak value of 1485.6 mA h g^{-1}. Additionally, the discharge specific capacity and coulombic efficiency can still be maintained at 1241.6 mA h g^{-1} and 100.3%, respectively, after 600 cycles, significantly outperforming CTS–Fe–C-1400 (862.6 mA h g^{-1} and 99.4%), CTS–Fe–C-1000 (710.4 mA h g^{-1} and 98.2%) and TF–Fe–C (532.4 mA h g^{-1} and 95.4%) LIBs. As seen from Fig. S25,† the CTS–Fe–C-1800 LIB can still exhibit a discharge specific capacity of 801.2 mA h g^{-1} after 1000 cycles at 1.0 A g^{-1}. This value surpasses that reported in the majority of previous literature studies, as illustrated in Table S4,† highlighting the good cycling stability of the CTS–Fe–C-1800 electrode. To further investigate the CTS–Fe–C-1800 electrode, a series of characterization studies were performed on the cycled electrode. XRD (Fig. S26a†) and SEM (Fig. S27a and b†) analyses demonstrated that the morphology and chemical structure of the electrode remained essentially unchanged before and after cycling. Furthermore, XPS (Fig. S26b–d†) analysis revealed the appearance of a CO_3^{2-} peak in the C 1s spectrum of the cycled electrode, attributed to Li_2CO_3, confirming the presence of a SEI film.[53] The SEI film is also directly observable in the TEM image (Fig. S27c†) of the cycled electrode.

The electrochemical reaction kinetic properties of CTS LIBs were further investigated based on the CV curves. The calculated *b* values corresponding to the anodic peaks of Fe–C LIBs are 0.95 (CTS–Fe–C-1800 LIB), 0.91 (CTS–Fe–C-1400 LIB), 0.89 (CTS–Fe–C-1000 LIB) and 0.7 (TF–Fe–C) (Fig. 7f and S28†), respectively. The results illustrate that the electrochemical processes include both diffusion-controlled and capacitive-controlled behaviors.[54] According to Fig. 7g, h and S29,† the percentage of the pseudocapacitance contribution of the CTS–Fe–C-1800 LIB increases from 67.4% to 85.0% as the scan rate increases from 1 mV s^{-1} to 20 mV s^{-1}, which is higher than that of the other samples. The prominent proportion of capacitive behavior of the CTS–Fe–C-1800 LIB is due to to its ion-accessible hierarchical pore structure and more active sites of Fe_3C NPs,[51] both of which facilitate ion diffusion. This is verified by the smallest Rs values of the CTS–Fe–C-1800 LIB as shown in Fig. 7i.

Finally, the rate performance of the CTS–Fe–C-1800 LIB was further investigated. As shown in Fig. 7j, the CTS–Fe–C-1800 LIB exhibits higher discharge specific capacity than the remaining LIBs at 0.1 A g^{-1}, 0.2 A g^{-1}, 0.4 A g^{-1}, 0.6 A g^{-1}, 0.8 A g^{-1}, 1.0 A g^{-1}, and 2.0 A g^{-1} current densities. Even at a high current density of 2.0 A g^{-1}, the CTS–Fe–C-1800 LIB can maintain a discharge specific capacity of 756.8 mA h g^{-1}. As a comparison, the CTS–Fe–C-1400 LIB, CTS–Fe–C-1000 LIB and TF–Fe–C LIB possess much lower discharge capacities of 598.7 mA h g^{-1}, 466.5 mA h g^{-1}, and 332.2 mA h g^{-1}, respectively. When the current density was changed to 0.1 A g^{-1}, the discharge specific capacity of the CTS–Fe–C-1800 LIB also recovers to 1466.3 mA h g^{-1}. The good rate performance of the CTS–Fe–C-1800 LIB could be attributed to the following factors: the smaller and more uniformly distributed Fe_3C NPs could enhance the efficiency of lithium-ion intercalation and deintercalation, and the porous carbon matrix helps relieve volume expansion.[49]

4 Conclusions

In this work, using the carbothermal shock method (1 second to 1800 °C), the iron-cellulose precursor was successfully transformed into a Fe-based carbon hybrid material, CTS–Fe–C-1800. The Fe-based NPs in CTS–Fe–C-1800 are uniformly distributed within a porous carbon matrix. The pyrolysis process of CTS generates a significant amount of organic small-molecule vapors, which serves as pore-forming agent, converting cellulose into a porous carbon matrix and preserving it. Simultaneously, the domain formed between the vapors precisely limits the growth of the Fe-based NPs. MD simulation calculations and mass loss data show that with increasing reaction temperature, the generation of small molecule gases increases significantly. Consequently, CTS–Fe–C-1800 exhibits the highest pyrolysis mass loss, indicating the most significant vapor generation. BET analysis further verifies this conclusion, showing that CTS–Fe–C-1800 has the highest specific surface area, indicating that it contains the highest number of pores created by gas generation. SEM and TEM images directly show that CTS–Fe–C-1800 exhibits the most porous morphology and the smallest Fe-based NPs. Notably, all NPs are confined to small domains divided by pores. XRD and Raman results reveal that CTS–Fe–C-1800 exhibits a higher degree of graphitization compared to CTS–Fe–C-1400 and CTS–Fe–C-1000. These characteristics facilitate efficient mass and ion transport when it was used as an electrode material. As a SC electrode, CTS–Fe–C-1800 exhibits a high specific capacity of 425.5 F g^{-1} at 0.5 A g^{-1}. The CTS–Fe–C-1800 flexible MSC achieves an energy density of 71.49 W h kg^{-1} at a power density of 0.637 kW kg^{-1}. Additionally, in LIB applications, CTS–Fe–C-1800 maintains a high specific

capacity of 801.2 mA h g^{-1} after 1000 cycles at a current density of 1 A g^{-1}.

Data availability

The data that support the findings of this study are available from the corresponding author, Heng Deng, upon reasonable request.

Author contributions

Jun Cao and Kaiyue Ji designed the experiments, and performed the material synthesis and characterization experiments. Minghe Du provided comments on the manuscript and supported the research of Jun Cao. Chi Zhang and Qi Sun provided detailed comments on the manuscript. Ying Yi and Zefan Chai assisted with partial characterization experiments. Chunjie Yan conducted the Raman and TEM measurements of the samples. All authors reviewed and commented on the manuscript. Heng Deng oversaw all research phases and provided regular guidance to the research. Jun Cao and Heng Deng wrote the manuscript. All authors discussed and commented on the manuscript.

Conflicts of interest

The authors declare no competing financial interests or personal relationships that could have influenced the work reported in this paper.

Acknowledgements

This work was supported by the National Natural Science Foundation of China (Grant No. 52303163), Guangdong Basic and Applied Basic Research Foundation (Grant No. 2022A1515110026), "CUG Scholar" Scientific Research Funds at China University of Geosciences (Wuhan) (Project No. 2022010) and Fundamental Research Funds for the Central Universities, China University of Geosciences (Wuhan) (No. CUG240613).

References

1 M. Chen, Y. Zhang, G. Xing, S.-L. Chou and Y. Tang, *Energy Environ. Sci.*, 2021, **14**, 3323–3351.
2 H. Zhao and Y. Lei, *Adv. Energy Mater.*, 2020, **10**, 2001460.
3 P. Dubey, V. Shrivastav, T. Boruah, G. Zoppellaro, R. Zbořil, A. Bakandritsos and S. Sundriyal, *Adv. Energy Mater.*, 2024, 2400521.
4 S. Zhao, B. Han, D. Zhang, Q. Huang, L. Xiao, L. Chen, D. G. Ivey, Y. Deng and W. Wei, *J. Mater. Chem. A*, 2018, **6**, 5733–5739.
5 H. Yang, H. Huang, Q. Wang, L. Shang, T. Zhang and S. Wang, *J. Mater. Chem. A*, 2023, **11**, 6191–6197.
6 H. Peng, W. Xiong, Z. Yang, J. Tong, M. Jia, Y. Xiang, S. Sun and Z. Xu, *Chem. Eng. J.*, 2023, **457**, 141317.
7 L.-L. Zhang, Z.-L. Wang, D. Xu, X.-B. Zhang and L.-M. Wang, *Int. J. Smart Nano Mater.*, 2013, **4**, 27–46.
8 W. Jiang, X. Zhang, X. Gong, F. Yan and Z. Zhang, *Int. J. Smart Nano Mater.*, 2010, **1**, 278–287.
9 Y. Arafat, M. R. Azhar, Y. Zhong, R. O'Hayre, M. O. Tadé and Z. Shao, *J. Mater. Chem. A*, 2023, **11**, 12856–12865.
10 Q. Liang, S. Wang, Y. Yao, P. Dong and H. Song, *Adv. Funct. Mater.*, 2023, **33**, 2300825.
11 B. B. Kopuklu, A. Tasdemir, S. A. Gursel and A. Yurum, *Carbon*, 2021, **174**, 158–172.
12 F. Wang, X. Wen, U. Mittal, R. K. Nekouei, T. Foller, Y. Shang, A. Bhadra, D. Chu, N. Sharma and D. Kundu, *Carbon*, 2024, **222**, 119003.
13 W. Tian, H. Zhang, X. Duan, H. Sun, G. Shao and S. Wang, *Adv. Funct. Mater.*, 2020, **30**, 1909265.
14 M. Jiang, J. Chen, Y. Zhang, N. Song, W. Jiang and J. Yang, *Adv. Sci.*, 2022, **9**, 2203162.
15 H. Liu, W. Zhang, W. Wang, G. Han, J. Zhang, S. Zhang, J. Wang and Y. Du, *Small*, 2023, **19**, 2304264.
16 H. Liu, K.-s. Moon, J. Li, Y. Xie, J. Liu, Z. Sun, L. Lu, Y. Tang and C.-P. Wong, *Nano Energy*, 2020, **77**, 105058.
17 S. Shen, Y. Chen, J. Zhou, H. Zhang, X. Xia, Y. Yang, Y. Zhang, A. Noori, M. F. Mousavi and M. Chen, *Adv. Energy Mater.*, 2023, **13**, 2204259.
18 D. Han, G. Guo, Y. Yan, T. Li, B. Wang and A. Dong, *Energy Storage Mater.*, 2018, **10**, 32–39.
19 J. Gao, X. Yan, C. Huang, Z. Zhang, X. Fu, Q. Chang, F. He, M. Li and Y. Li, *Angew. Chem., Int. Ed.*, 2023, **135**, e202307874.
20 Y. Cui, W. Feng, W. Liu, J. Li, Y. Zhang, Y. Du, M. Li, W. Huang, H. Wang and S. Liu, *Nanoscale*, 2020, **12**, 10816–10826.
21 Y. Zhao, L. P. Wang, M. T. Sougrati, Z. Feng, Y. Leconte, A. Fisher, M. Srinivasan and Z. Xu, *Adv. Energy Mater.*, 2017, **7**, 1601424.
22 W. Guo, W. Sun, L.-P. Lv, S. Kong and Y. Wang, *ACS Nano*, 2017, **11**, 4198–4205.
23 T. Hou, B. Liu, X. Sun, A. Fan, Z. Xu, S. Cai, C. Zheng, G. Yu and A. Tricoli, *ACS Nano*, 2021, **15**, 6735–6746.
24 J. Jin, Z. Wang, R. Wang, J. Wang, Z. Huang, Y. Ma, H. Li, S. H. Wei, X. Huang and J. Yan, *Adv. Funct. Mater.*, 2019, **29**, 1807441.
25 K. Zhou, M. Hu, Y. He, L. Yang, C. Han, R. Lv, F. Kang and B. Li, *Carbon*, 2018, **129**, 667–673.
26 J. Yin, W. Zhang, N. A. Alhebshi, N. Salah and H. N. Alshareef, *Small Methods*, 2020, **4**, 1900853.
27 M. Li, H. Du, L. Kuai, K. Huang, Y. Xia and B. Geng, *Angew. Chem., Int. Ed.*, 2017, **56**, 12649–12653.
28 C. H. Dreimol, H. Guo, M. Ritter, T. Keplinger, Y. Ding, R. Günther, E. Poloni, I. Burgert and G. Panzarasa, *Nat. Commun.*, 2022, **13**, 3680.
29 P. Jing, Q. Wang, B. Wang, X. Gao, Y. Zhang and H. Wu, *Carbon*, 2020, **159**, 366–377.
30 O. Senneca, F. Cerciello, C. Russo, A. Wütscher, M. Muhler and B. Apicella, *Fuel*, 2020, **271**, 117656.
31 L. He, H. Wu, W. Zhang, X. Bai, J. Chen, M. Ikram, R. Wang and K. Shi, *J. Hazard. Mater.*, 2021, **405**, 124252.
32 Z. Zhuang, B. Guan, J. Chen, C. Zheng, J. Zhou, T. Su, Y. Chen, C. Zhu, X. Hu and S. Zhao, *Chem. Eng. J.*, 2024, 150374.

33 C. Jin, J. Nai, O. Sheng, H. Yuan, W. Zhang, X. Tao and X. W. D. Lou, *Energy Environ. Sci.*, 2021, **14**, 1326–1379.
34 J. Cao, C. Yan, Z. Chai, Z. Wang, M. Du, G. Li, H. Wang and H. Deng, *J. Colloid Interface Sci.*, 2024, **653**, 606–616.
35 W. Song, J. Zhu, B. Gan, S. Zhao, H. Wang, C. Li and J. Wang, *Small*, 2018, **14**, 1702249.
36 J. Wang, Q. Li, J. Ren, A. Zhang, Q. Zhang and B. Zhang, *Carbon*, 2021, **181**, 28–39.
37 B. Deng, Z. Wang, W. Chen, J. T. Li, D. X. Luong, R. A. Carter, G. Gao, B. I. Yakobson, Y. Zhao and J. M. Tour, *Nat. Commun.*, 2022, **13**, 262.
38 T.-H. Kim, G.-T. Gong, B. G. Lee, K.-Y. Lee, H.-Y. Jeon, C.-H. Shin, H. Kim and K.-D. Jung, *Appl. Catal., A*, 2006, **305**, 39–45.
39 Z. Zeng, H. Zhao, J. Wang, P. Lv, T. Zhang and Q. Xia, *J. Power Sources*, 2014, **248**, 15–21.
40 D. Chen, C. Feng, Y. Han, B. Yu, W. Chen, Z. Zhou, N. Chen, J. B. Goodenough and W. He, *Energy Environ. Sci.*, 2020, **13**, 2924–2937.
41 K. O. Otun, Y. Yao, X. Liu and D. Hildebrandt, *Fuel*, 2021, **296**, 120689.
42 E. Thompson, A. Danks, L. Bourgeois and Z. Schnepp, *Green Chem.*, 2015, **17**, 551–556.
43 B. J. Mapleback, T. J. Simons, Y. Shekibi, K. Ghorbani and A. N. Rider, *Electrochim. Acta*, 2020, **331**, 135233.
44 W. Li, Y. Tang, W. Kang, Z. Zhang, X. Yang, Y. Zhu, W. Zhang and C. S. Lee, *Small*, 2015, **11**, 1345–1351.
45 P. Lu, Y. Sun, H. Xiang, X. Liang and Y. Yu, *Adv. Energy Mater.*, 2018, **8**, 1702434.
46 C.-T. Toh, H. Zhang, J. Lin, A. S. Mayorov, Y.-P. Wang, C. M. Orofeo, D. B. Ferry, H. Andersen, N. Kakenov and Z. Guo, *Nature*, 2020, **577**, 199–203.
47 Q. Zhang, E. Uchaker, S. L. Candelaria and G. Cao, *Chem. Soc. Rev.*, 2013, **42**, 3127–3171.
48 Y. Liu, X. Xu and Z. Shao, *Energy Storage Mater.*, 2020, **26**, 1–22.
49 L. Wang, J. Han, D. Kong, Y. Tao and Q.-H. Yang, *Nano-Micro Lett.*, 2019, **11**, 1–23.
50 M. B. Poudel and H. J. Kim, *Chem. Eng. J.*, 2022, **429**, 132345.
51 L. Hou, W. Yang, X. Xu, B. Deng, Z. Chen, S. Wang, J. Tian, F. Yang and Y. Li, *Chem. Eng. J.*, 2019, **375**, 122061.
52 Y. Zuo, G. Wang, J. Peng, G. Li, Y. Ma, F. Yu, B. Dai, X. Guo and C.-P. Wong, *J. Mater. Chem. A*, 2016, **4**, 2453–2460.
53 G. Zhang, X. Wei, G. Han, H. Dai, J. Zhu, X. Wang, X. Tang and J. Ye, *J. Power Sources*, 2021, **484**, 229312.
54 D. Xiao, Q. Li, H. Zhang, Y. Ma, C. Lu, C. Chen, Y. Liu and S. Yuan, *J. Energy Storage*, 2017, **5**, 24901–24908.

